Tailor-Made Charged Catechol-Based Polymeric Ligands to Build Robust Fuel Cells Containing Antioxidative Nanoparticles

Hyunhong Kim, Seung Ho Yook, Ho Young Kim, Yonghoon Choi, Yeongsu Lim, Yujin Hwang, Jeongho Kim, Kwan Young Lee, Seung Soon Jang, Jongnam Park,* and Jin Young Kim*

Cerium oxide nanoparticles (CNPs) are investigated as radical scavengers to increase the durability of polymer electrolyte membrane fuel cells (PEMFCs). However, the practical application of CNPs in PEMFCs is hindered by the low stability of the CNPs during cell operation and the low compatibility of the CNPs with PEM. In this study, as effective antioxidants for PEMs, surface-engineered CNPs, passivated with dopamine-based copolymer ligands containing multidentate catechol pendant groups (CNP@DPLs), are reported. The DPLs provide enhanced colloidal and chemical stability in acidic and radical environments, thanks to the robust catechol binding groups and polymer backbone shielding. It is highlighted that they also improved the redox cycling ability of the CNPs, with catechol's additional radical scavenging. Using the CNP@DPLs as a model system, the effect of surface charge is also examined. Negatively charged sulfonic acid-functionalized CNPs (CNP@DSAs) exhibit the highest compatibility with PEMs. Coherently, the CNP@DSA-based reinforced composite membrane (CNP@DSA-RCM) shows the lowest disintegration rate in Fenton's test. The PEMFC based on the CNP@DSA-RCM outperforms previously reported antioxidant-based PEMFCs. Importantly, while the pristine PEMFC and Ce salt-based one undergoes degradation after 40 h, the CNP@DSA based PEMFC retains its performance even after 100 h.

1. Introduction

Polymer electrolyte membrane fuel cells (PEMFC) are becoming one of the most attractive eco-friendly energy devices in the transition period from fossil fuel to hydrogen-based society, because of their high energy conversion efficiency and near-zero emissions.[1] Tremendous effort has been invested in developing and optimizing PEMFC-powered automobiles, power generators, ships, and drones. Today the most serious obstacle to the broader use of PEMFCs is the lifespan of the fuel cell, which is strongly affected by membrane durability. Perfluorinated sulfonic acid (PFSA) is the most commonly used electrolyte membrane in PEMFCs because of its high proton conductivity and mechanical/thermal stability.[2] However, the PFSA membrane can be significantly decomposed by radicals such as the hydroxyl radical (HO·) and hydroperoxyl radical (HOO·), generated during the electrochemical process.

H. Kim, Y. Choi, J. Park
Department of Biomedical Engineering
School of Energy and Chemical Engineering
Ulsan National Institute of Science and Technology (UNIST)
Ulsan 44919, Republic of Korea
E-mail: jnpark@unist.ac.kr

The ORCID identification number(s) for the author(s) of this article can be found under https://doi.org/10.1002/aelm.202200171.

S. H. Yook, H. Y. Kim, J. Y. Kim
Hydrogen Fuel Cell Research Center
Korea Institute of Science and Technology (KIST)
14-gil 5 Hwarang-ro, Seongbuk-gu, Seoul 02792, Republic of Korea
E-mail: jinykim@kist.re.kr

S. H. Yook, K. Y. Lee, J. Y. Kim
Department of Chemical and Biological Engineering
Korea University
145 Anam-ro, Seongbuk-gu, Seoul 02841, Republic of Korea

Y. Lim, Y. Hwang, J. Kim
Department of Chemistry and Chemical Engineering
Inha University
100 Inha-ro, Michuhol-gu, Incheon 22212, Republic of Korea

S. S. Jang
School of Materials Science and Engineering
Georgia Institute of Technology
771 Ferst Drive, N.W. Atlanta, GA 30332-0245, USA

One notable way to mitigate the radical-mediated degradation is to fabricate reinforced composite membranes (RCMs) containing nano-antioxidant additives.[3–6] Nanomaterials with reversible redox cycling behavior can efficiently scavenge radicals, preventing PEM disintegration. Ce ions have been widely used as radical scavengers to enhance PFSA membranes based on their reversible redox cycling behavior between Ce(III) and Ce(IV). However, the migration of Ce ions during PEMFC operation often severely degrades performance by contaminating the catalyst layer and reducing the proton conductivity of the PFSA membrane.[7–12] To address this, ceria nanoparticles (CNPs) have been employed as additives in PFSA membranes because of their superior antioxidant activity to bulk materials derived from the multivalent nature and immobilization properties on the membrane.[13] Their good water adsorption properties, from the hydroxyl groups on the CNPs, are also beneficial to the durability of the PEMFC in dry conditions because they enhance proton conductivity and hinder the generation of cracks in the membrane.[14–16] PEMFC operation and membrane fabrication are performed in aqueous phases, so the hydrophilic NP surface is a primary requirement for using CNPs in PEMs.

Because of their large surface-to-volume ratio, the surface of the NPs dominates their physicochemical properties,[17] especially water retention, colloidal stability, and the passivation of the CNPs against attacking molecules and mechanical interaction with composites.[13–16,18,19] Despite progress using CNPs-containing PFSA membranes in PEMFCs, surface engineering of the CNPs for PEMFCs has been limited.[20] The relationship between PEMFC performance and the CNP surface properties is not fully understood, and surface engineering techniques for the CNPs are lacking.

Catecholic amino acids such as dopamine, which is secreted by marine mussels, are well-established surface modifiers because of their ability to bind to transition metal oxide NPs, including iron, zinc, and titanium, in harsh seawater conditions. Lots of studies have used catechol-appended ligands to provide water solubility to transition metal oxide NPs.[21,22] However, reliable coating methods have not been achieved with rare-earth metal oxide NPs, including CNPs. Not only colloidal stability but also enhanced radical scavenging activities can be expected from dopamine derivatives with tethered ligands because catechol is a representative antioxidant.[23–25]

In this study, we report surface-engineered CNPs with enhanced colloidal stability, chemical durability, radical scavenging activity, and water retention using dopamine-based polymeric ligands (DPLs) with tunable surface charge. We prepared negatively, neutrally, and positively charged CNPs using sulfonic acid (DSA), polyethylene glycol (DmP), and trimethylammonium (DTMA) groups, respectively. We established the relationship between the surface charge of the CNPs and PEMFC performance by exploring the physicochemical properties of each CNP. In Fenton's test, the CNP@DPL-based RCMs had much lower fluoride emission rates (FERs) than the pristine membrane and the industrial Ce salt-based RCM, demonstrating the excellent antioxidation efficiency of the CNP@DPLs. Among the various prepared CNP@DPLs, the negatively charged CNP@DSA demonstrated excellent compatibility with PEMs, showing high performance that rivaled

pristine RCM in the PEMFC test. Notably, the PEMFC performance of CNP@DSA-RCM surpassed those of previously reported antioxidant-based PEMFCs, confirming that the CNP@DSA had superior antioxidation efficiency. More importantly, the CNP@DSA-RCM retained its performance for 100 h in a durability test, while the pristine one suffered from severe deactivation after 40 h.

2. Results and Discussion

2.1. Synthesis of the CNP@DPL via Surface Passivation

The CNP@DPL samples were prepared via the ligand exchange method (**Figure 1**a). We first prepared oleic acid-capped ceria nanoparticles (CNP@OA) with a solvothermal reaction.[26] As shown in the high-resolution transmission electron microscopy (TEM) image of CNP@OA (Figure S1a, Supporting Information), the average diameter of NPs is 4.6 ± 0.6 nm. The selected area diffraction (SAED) patterns consisted of (111), (200), (220), and (311) Debye–Scherrer rings with the corresponding d-spacing of 0.32, 0.28, and 0.17 nm.[27] The X-ray diffraction (XRD) patterns of CNP@OA (Figure S1b, Supporting Information) also corroborate (111), (200), (220), (311), and (222) planes of cubic fluorite CeO_2 structure (JCPDS 34-0394).[28]

To confer the environmental compatibility of the CNP@OA in polar media such as the PFSA-based membrane, we passivated the surface of the CNP@OA with various charge-modulated DPLs. The DPLs were synthesized using the reversible addition-fragmentation chain-transfer (RAFT) polymerization method (Figure S2, Supporting Information), which has merits of a controllable degree of polymerization (DP), a diverse functionalization, and a narrow polydispersity (PDI). We synthesized catechol-based, tailor-made charged polymers with the same backbone using three different hydrophilic groups. The positively charged DPL was synthesized using the trimethylammonium group (dopamine-based trimethyl ammonium polymeric ligands; DTMA) (Figure 1b). The preparation of the neutral DPL was performed using the poly(ethylene glycol) group [dopamine-based poly(ethylene glycol) methyl ether polymeric ligands; DmP] (Figure 1c). The negatively charged one was prepared using a sulfonic acid group (dopamine-based sulfonic acid polymeric ligands; DSA) (Figure 1d). These hydrophilic functional groups are well-known NP surface stabilizers in chemical/biological applications because they provide steric hindrance and charged repulsive force to the NPs, enhancing colloidal stability. The ^1H nuclear magnetic resonance (NMR) spectra of the DPLs indicated polymerization was successful (Figure S3, Supporting Information). All of the polymeric ligands had similar DPs of about 25 and catechol group contents of about 20%. The ratio of dopamine moiety, hydrophilic groups, molecular weight, DP, and PDI are summarized in Table S1 (Supporting Information).

Then, we exchanged the ligand in the CNP@OA with the prepared DPLs, using 2-(2-aminoethoxy)ethanol (AEE) additives.[29] As shown in Figure S4 (Supporting Information), the yellow-colored CNP colloidal dispersion transferred from toluene (the top layer) into water (bottom layer), implying successful ligand exchange reactions occurred between the OA and DPLs.
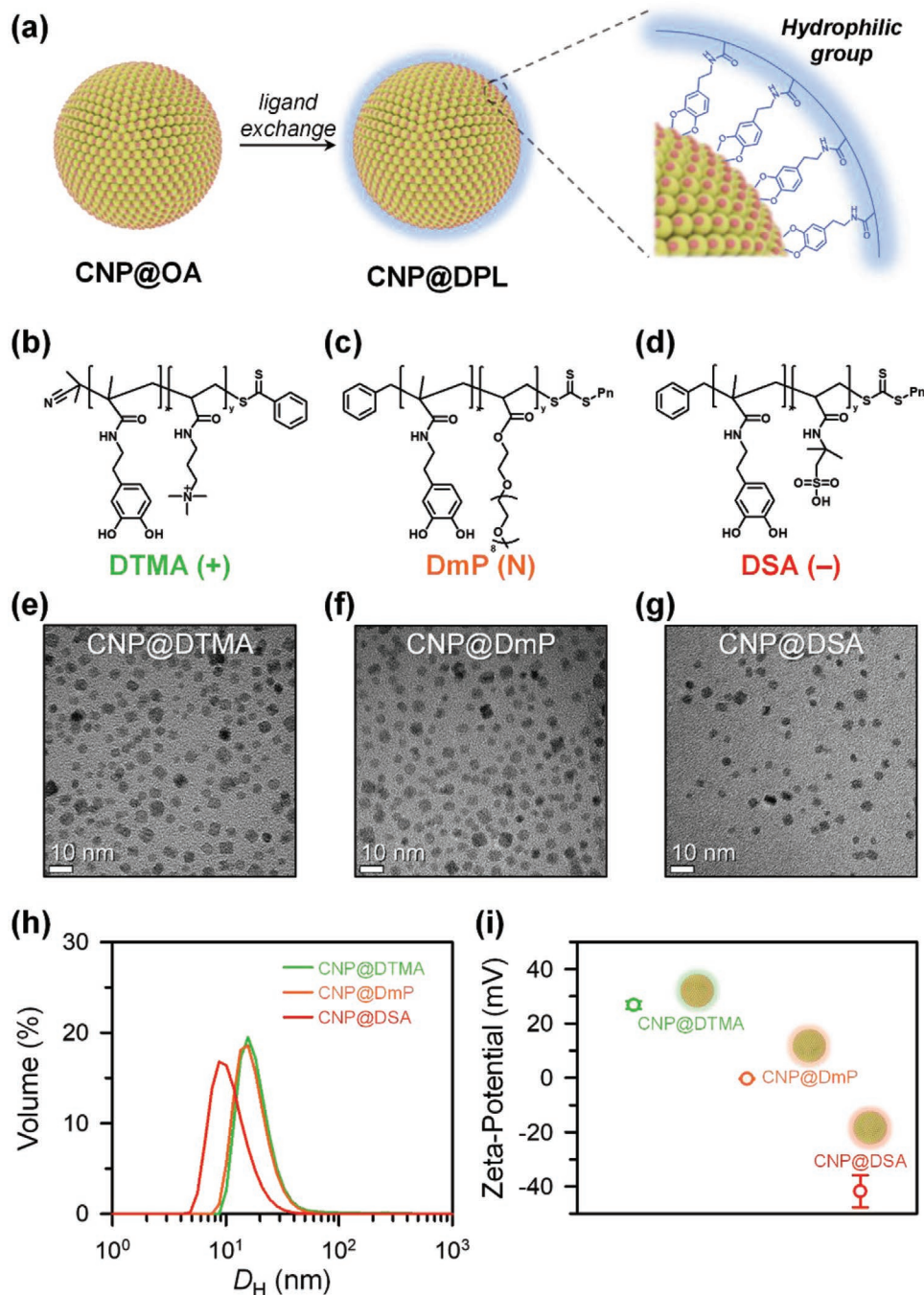
Figure 1. Preparation of CNP@DPLs. a) Schematic illustration for the synthesis of CNP@DPLs via ligand exchange method. Molecular structures of b) positively charged DTMA, c) neutrally charged DmP, and d) negatively charged DSA. TEM images of e) CNP@DTMA, f) CNP@DmP, and g) CNP@ DSA. h) Particle size distribution of CNP@DPLs taken from the DLS measurement. i) Zeta potential of CNP@DPLs. Insets are illustration models for each CNP@DPL.

The result indicates that a successful ligand exchange reaction occurred with the CNPs with the three DPL, proving that the catecholic group can be an efficient anchor group for the CNPs. This is noteworthy because most previous papers about catecholic ligands have focused on surface engineering for transition metal oxide NPs.[30–33] After surface modification, the sizes of the CNP@DTMA (4.2 ± 1.1 nm), DmP (4.2 ± 0.9 nm), and

DSA (4.4 ± 1.0 nm) were virtually identical (Figure 1e–g). Also, TEM images confirmed the NPs were evenly dispersed, without agglomeration. A slight change in the morphology of the CNPs was observed after the surface modification. This phenomenon might be attributed to ligand-induced surface etching due to the high binding affinity of catechol to CNPs.[34–36] We also estimated the hydrodynamic diameter (D_H) of the CNP@DPL samples

ADVANCED
SCIENCE NEWS
www.advancedsciencenews.com

ADVANCED
ELECTRONIC
MATERIALS
www.advelectronicmat.de

using dynamic light scattering (DLS) measurements. As shown in Figure 1h, the D_H of the CNP@DTMA, CNP@DmP, and CNP@DSA were 19.4, 17.7, and 11.4 nm, respectively. Regardless of the hydrophilic group, the aqueous dispersions of the CNP@DPL samples exhibited narrow monomodal curves for size distribution, indicating successful CNP passivation by DPLs. This individual stabilization of CNPs originates from the amine-assisted catechol nanocoating mechanism (Figure S5, Supporting Information).[29] Since catechol acts as a hard Lewis base, it coordinates effectively with Ce(IV) species, whose Lewis acidity is stronger than Ce(III).[37] During the ligand exchange step with AEE, the amine groups from the AEE combine with catechol in the DPLs. The in situ-generated catechol-amine complexes reduce the oxidized quinone group, resulting in the formation of a robust DPL monolayer on the CNPs.[29] In contrast, without AEE, the Ce(IV)-catechol complex produces semi-quinone via an oxidase-like process by the CNPs, and the DPLs are finally detached from the CNP surface.[38,39]

The zeta-potential data of the CNP@DPL samples further demonstrated that our sample preparation was successful. Following our design principle for the charged polymer, the zeta-potential values of the CNP@DTMA, CNP@DmP, and CNP@DSA were +27, -0.4, and -42 mV, respectively (Figure 1i).

2.2. Physicochemical Properties of Charged CNP@DPLs

We scrutinized the physicochemical properties of the CNPs following the DPL passivation. To build up reference data, we also characterized tetradecyltrimethylammonium bromide-capped ceria nanoparticles (CNP@TTAB). TTAB is a capping agent widely used to prepare polar solvent-based NP dispersions, and comparing the CNP@DPLs with CNP@TTAB could help clarify the effect of the catechol group on the physicochemical properties. We first investigated how the DPLs affected the chemical stability of the CNPs. It is well known that CNPs are prone to disintegrate in PEMFC operating conditions, which include abundant radical species and a harsh acidic environment (about pH -0.5). The deteriorated CNPs inside the PEM cause Ce ionic migration and significantly degrade PEMFC performance.[40] To evaluate the chemical stability of the CNPs in acidic media, we used DLS analyses to measure the D_H of the CNPs in an acidic solution (pH = 2). The applied pH condition is milder than practical systems, but it is suitable for screening the chemically durable CNPs as the cerium species exist in the same Ce(III) state in the range of pH between 2 and -2.[41,42] As shown in **Figure 2**a, the changes in particle size over time clearly suggest the superior stability of the CNP@DPL samples over CNP@TTAB. After the stability test, the CNP@TTAB underwent a drastic decrease in particle size, indicating that CNP suffered from metal dissolution. In contrast, the initial D_H values of the CNP@DPL samples were virtually identical during the test, up to 96 h. This was due to the suppression of Ce dissolution by the robust DPL monolayer generated by surface passivation. In addition, to test their resistance against radical attacks, we measured the temporal D_H of the CNPs in Fenton's reagent (2 wt% H_2O_2 solution containing 3 ppm of Fe(II) ion). As shown in Figure 2b, the CNP@DPLs retained their initial D_H even after 96 h, while the CNP@TTAB underwent enlargement

of D_H, suggesting colloidal dispersibility was degraded due to particle agglomeration. We note that the bonding structure of catechol-metal complexes further enhanced the stability of CNPs against Fenton's test. It is generally accepted that the free catechol motifs are vulnerable to oxidation.[43] In our study, once we generated catechol-metal complexes in CNP@DPLs, they were more robust against oxidation compared to free catechol groups. As a result, catechols bound on the CNPs are key for maintaining D_H of CNPs up to 96 h.

We also substantiated the beneficial ability of the DPLs to enhance the radical scavenging activity of the CNP. X-ray photoelectron spectroscopy (XPS) analyses revealed that surface passivation engineering increased the content of Ce(III), which are highly active sites for the radical scavenging process. The as-prepared CNP@OA contained 19.0% Ce(III) in its deconvoluted Ce3d XPS spectra (Figure S6, Supporting Information), while the CNPs after surface passivation possessed a much higher content of Ce(III) (Figure 2c and Figure S7, Supporting Information). The calculated ratios of Ce(III) were in the following order: CNP@DSA (40.5%) ≥ CNP@DmP (39.5%) ≥ CNP@DTMA (39.2%) > CNP@TTAB (28.3%). Because the CNP surface modification process also results in surface etching, the surface passivated CNPs undergo a slight reduction in particle size (Figure 1e-g). These smaller CNPs had higher Ce(III) ratios than as-prepared CNP@OA because they contained more oxygen vacancies and had higher degrees of lattice strain.[44] Furthermore, unlike TTAB, the catechol groups in the DPL partially assist the reduction of the CNP surface during the ligand exchange process. Although both the HO· scavenging process by Ce(III) and HOO· elimination by Ce(IV) are crucial to the antioxidation behavior of the CNPs, the Ce(III) fraction is considered to be more influential than Ce(IV) for catalase-like catalytic and superoxide dismutase mimicking activity.[14,44] The DPL coating results in the catechol-derived activation of CNPs, boosting the number of Ce(III) active sites in the CNP@DPLs.

We further tested the radical scavenging activity by measuring photoluminescence (PL) using 6-carboxyl fluorescein (6-CFL) fluorescent dye as a probe (Figure 2d). We chose CNP@DSA as a representative analyte because CNP@DSA exhibited the highest Ce(III) fraction in the XPS analyses. When the analytes contain hydroxyl radicals generated from the Fenton's reaction, 6-CFL degrades, and the PL intensity decreases. To compare the rate of decay in PL intensity of each solution, we plotted the temporal profiles of the PL intensities at 521 nm (Figure S8, Supporting Information). TTAB encapsulated CNPs were used as a reference because the sample had a hydrophobic protection layer on the NPs,[45] which can hamper the approach of aqueous radical ions to cerium ions on the NPs.[46,47] The overall PL intensities decayed over time for both CNPs. The time constants (τ) for the temporal decay of the PL intensity were determined by fitting with a single exponential function, $I(t) = Ae^{-t/\tau}$ (Figure 2d). The τ of CNP@DSA and CNP@TTAB were 77.8 and 42.6 min, respectively. Although the surface ligand on the CNP can interfere with the catalytic activity of the CNP by reducing the number of available catalytic sites and increasing the effective diffusion length of the radical to the CNP core, CNP@DSA was proven to have a higher radical scavenging property than CNP@TTAB. The compact coating layer of CNP@DSA is highly permeable to radicals, and
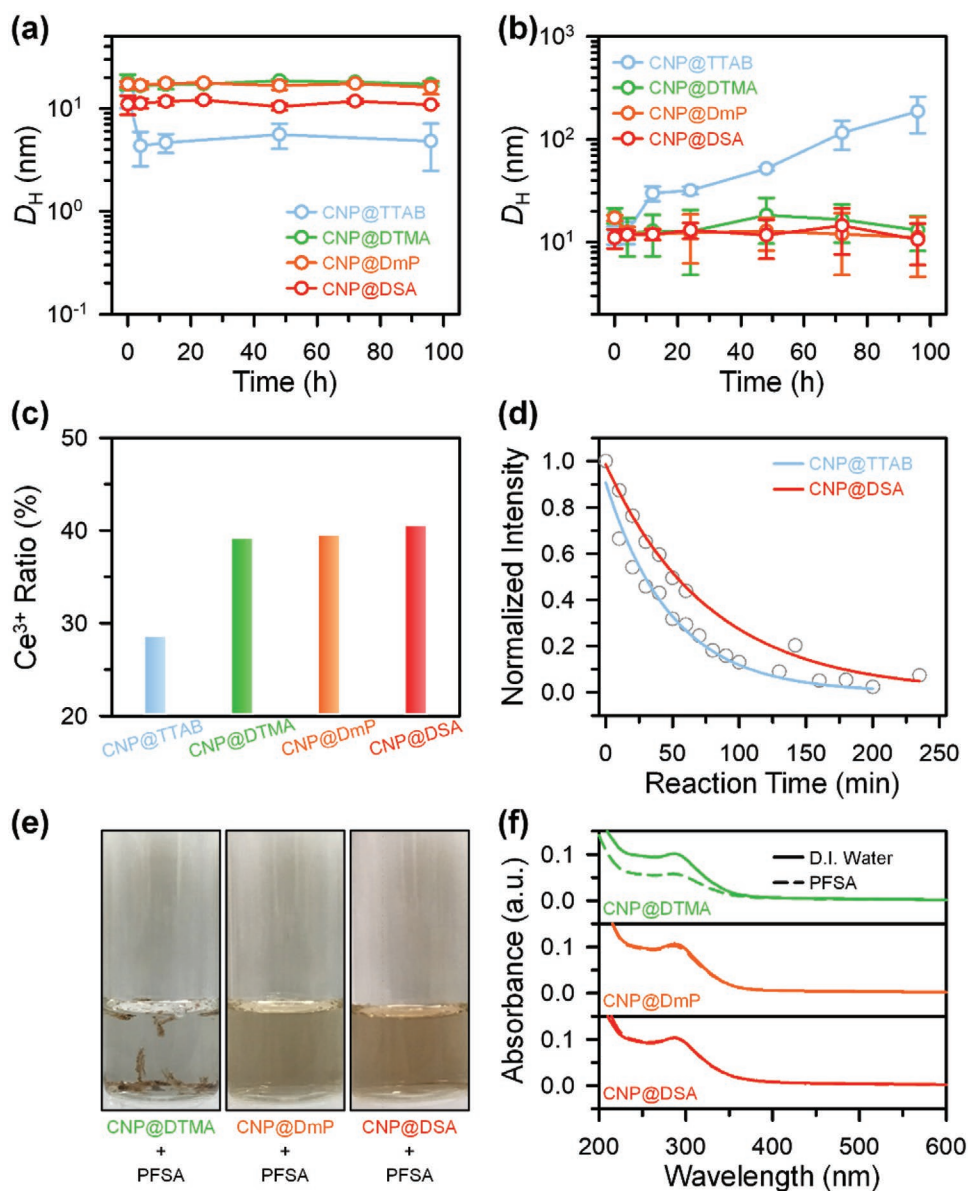
ADVANCED
SCIENCE NEWS
www.advancedsciencenews.com

ADVANCED
ELECTRONIC
MATERIALS
www.advelectronicmat.de

Figure 2. Physicochemical properties of CNP@DPLs. a,b) Temporal DLS results showing the changes in DH of CNPs in acidic solution and radical solution. c) Ce3d XPS results showing the ratio for the Ce(III) chemical state. d) Temporal decays of PL intensity at 521 nm emission wavelength for 6-CFL solution containing CNP@DSA and CNP@TTAB. e) Photographs of PFSA solutions containing each CNP@DPL. f) UV–vis spectra of CNP@DPL aqueous dispersions and CNP@DPL-PFSA solutions.

its hydrophilic nature promotes effective radical scavenging. Also, the DPL on the CNPs can induce a synergistic antioxidation process with the CNPs through the keto–enol tautomerization reaction.[24] The random copolymer structure of the DPL shell has several grafting modes depending on the surface curvature of CNPs, and the leftover unbounded dopamine pendant groups can provide additional radical scavenging abilities to the CNP surface.[48]

To gain a deeper insight into the enhanced antioxidation efficiency of the CNP@DPLs compared to CNP@TTAB, we performed colorimetric analysis using ultraviolet–visible spectroscopy (UV–vis).[13,44,49] As shown in the photographs in Figure S9 (Supporting Information), after adding the H_2O_2

solution, the color of the red-colored aqueous dispersion of the CNP@DSA sample turned yellow, implying the oxidation of Ce(III) into Ce(IV). Simultaneously, the UV–vis absorbance at 400 nm ($A_{400\ nm}$) increased. As the increase in $A_{400\ nm}$ depends on the concentration of the H_2O_2 solution,[49] we used $A_{400\ nm}$ as a qualitative probe of Ce (IV) contents (Figure S9, Supporting Information). We prepared H_2O_2 solutions of various concentrations and added them to the CNP aqueous dispersions. Then, we measured the time-dependent changes (1 min, 2 d, 4 d after addition) in the $A_{400\ nm}$ of the samples containing H_2O_2 solution and CNPs. As shown in Figure S10 (Supporting Information), 1 min after adding the H_2O_2 solutions, the $A_{400\ nm}$ values of the CNP@DSA rapidly increased, regardless of the H_2O_2

concentration (inverted triangles in Figure S10, Supporting Information). Over time, the $A_{400\ nm}$ values of the CNP@DSA began to continuously decrease (diamonds and regular triangles in Figure S10, Supporting Information), indicating regeneration of the Ce(IV) species on the CNP surface into the Ce(III) state.[49] In contrast, the CNP@TTAB exhibited virtually identical $A_{400\ nm}$ values during the colorimetric test, implying that the initial Ce(IV) contents were already abundant, and the reaction rate for the Ce(III) regeneration process was very sluggish. To gain more comprehensive information, we also tested a commercial CNP aqueous dispersion (Sigma-Aldrich). That CNP (Sigma-Aldrich) also showed immediate increases in $A_{400\ nm}$ after adding the H_2O_2 solution, but they exhibited a successive increase in $A_{400\ nm}$ values without recovery. This clearly suggests that the regeneration efficiency of the CNP (Sigma-Aldrich) is inferior to that of the CNP@DSA. As we had first speculated, we found that the DPLs can improve chemical stability and radical scavenging performance by generating abundant Ce(III) active sites and preventing the loss of Ce(III)-rich surfaces against various reaction environments.

Next, to examine the feasibility of each CNP@DPL as a radical scavenger additive for PEMs, we tested the colloidal stability of CNP@DPLs in a PFSA-rich environment. Mimicking the fabrication condition of the RCMs, we prepared a solution containing PFSA ionomer and CNP@DPL ($[Ce]/[SO_3^-]$ = 0.2 mol%). As shown in the photographs of the CNP@DPL-PFSA solution (Figure 2e), the CNP@DTMA showed poor colloidal stability in the PFSA solution. CNP@DTMA formed a significant agglomeration due to the electrostatic interaction between the positively charged ammonium group and the negatively charged PFSA ionomer. In contrast, the neutrally

charged DmP and negatively charged DSA proved to be compatible, preserving the individual passivation of the CNPs even in the PFSA solution. The UV–vis spectra (Figure 2f) also corroborated the colloidal stability of the CNP@DPLs in the PFSA solution. The CNP@DTMA underwent a dramatic decrease in absorbance after mixing with the PFSA solution, while there were no noticeable absorbance changes in the UV–vis spectra of the others. This indicates that the type of hydrophilic ligand materials in the capping agent should be selected carefully, as the colloidal stability of the CNPs highly depends on the charge of the surface stabilizer.

2.3. Characterization of CNP@DPL-Based RCMs

Next, we fabricated multilayered RCMs using the CNP samples as functional antioxidant additives (**Figure 3**a and Figure S11a, Supporting Information).[50] Briefly, we prepared a mixture containing the PFSA ionomer solution and an aqueous dispersion of the CNP samples. Then, a white-colored porous polytetrafluoroethylene (PTFE) film was immersed into the CNP-PFSA liquid mixture to form a transparent film. The thickness of the resulting CNP-containing RCMs was ≈20 µm (Figure S11b, Supporting Information). For benchmarks, we prepared RCMs containing Ce(III) salt, a widely used antioxidant. We also compared the properties of pristine RCM, fabricated without antioxidants.

We first investigated the mechanical properties of the RCMs based on the CNP samples (CNP-RCMs). We obtained the strain-stress curves of the RCMs under uniaxial extension (Figure S12, Supporting Information). Figure S12a (Supporting Information)
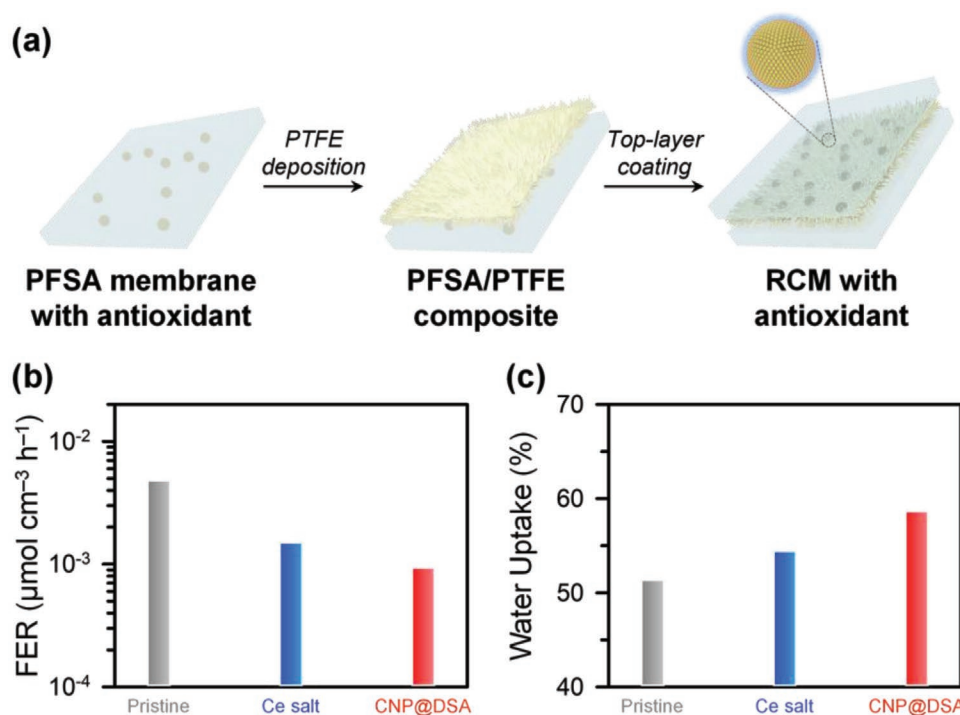

Figure 3. Fabrication of CNP-based RCMs. a) Schematic illustration of RCM fabrication. b) FERs of RCMs during the Fenton's test. c) Water uptakes of RCMs.

shows how the mechanical properties of the RCM change by CNP@DSA. The CNP@DSA-RCM exhibits lower yield stress than the pristine RCM and Ce(III) salt-based one, implying that the permanent deformation of CNP@DSA-RCM is intenser than others. Likewise, CNP@DTMA and CNP@DmP also showed decreased yield stress than the pristine RCM (Figure S12b, Supporting Information). Instead, the CNP@DPL-RCMs demonstrated enhanced maximum tensile strength and elongation at the break. Tensile strength and break strain of all CNP@DPL-RCM samples surpass pristine RCM, suggesting increases in ductility and toughness. These changes in mechanical properties can be attributed to the efficient CNP-PFSA interconnection induced by charge interaction. The CNP@DPLs effectively retard failure because they can link between PFSA/PTFE polymer backbones. Furthermore, under stress, the CNP@DPLs undergo rearrangement and exchange processes of the polymers on the CNP surface, resulting in modification of the mechanical properties by dissipating energy.[51]

To assess the radical scavenging performance of the prepared RCMs, we performed the Fenton's test, which is a well-known accelerated chemical degradation test protocol (Figure 3b).[52] Exposing RCMs to Fenton's reagent continuously generates hydroxyl radicals, and the radical-mediated decomposition of the RCMs leads to an emission of fluoride ions from the PTFE backbones. Then, we quantified the emission rate of the fluoride ions (FER) to determine the degree of RCM degradation. As shown in Figure 3d, the pristine RCMs exhibited the highest FER value (4.8 nmol cm^{-2} h^{-1}), indicating the fastest membrane disintegration. This also suggests that the addition of an antioxidant mitigates membrane degradation. Of the CNP@DSA-RCM and Ce(III) salt-RCM, the CNP@DSA-RCM exhibited a lower FER value (0.93 nmol cm^{-2} h^{-1}) than the Ce(III) salt-based sample (1.5 nmol cm^{-2} h^{-1}), confirming its superior chemical durability. Interestingly, each CNP@DPL sample showed nearly identical FERs under the same test conditions (Figure S13, Supporting Information). These results confirm the additional radical scavenging via catechol groups on the CNPs, as demonstrated by XPS, PL, and UV–vis analyses.[53,54]

We also investigated the water uptake of the prepared RCMs (Figure 3c). The amount of water adsorbed in the RCMs is one of the pivotal factors affecting proton conduction during PEMFC operation. The proton conductivity increases in humid conditions as water increases the interconnectivity of ionic clusters and the phase homogeneity of the PFSA, resulting in an extended proton diffusion length.[15,55] The water uptakes of the pristine RCM, Ce(III) salt-RCM, and CNP@DSA-RCM were 51.3%, 54.4%, and 58.6%, implying that the CNP@DSA can facilitate proton migration in the RCM. Moreover, CNP@DTMA-RCM and CNP@DmP-RCM showed water uptakes of 56.2% and 58.4%, respectively, proving that the DPLs assisted the high-water retention in the RCMs (Figure S14, Supporting Information). This can be attributed to the hydrophilic groups in the DPLs. It is well known that the surface characteristics of additive particles can significantly affect the water adsorption property of a membrane and the water management of the entire fuel cell system.[15,16] In terms of membrane water management during PEMFC operation, among the CNP@DPL samples, it is expected that the CNP@DSA will be

the most suitable, as negatively charged carboxyl groups have been shown to possess the highest binding energy to water, due to the formation of a double hydrogen bond.[56]

2.4. Cell Performance of the RCM-Based PEMFCs

Finally, we tested the PEMFC performance of the RCMs. The PEMFC test was conducted based on the membrane electrode assemblies (MEAs) at 80 °C with 50% relative humidity (RH), reflecting the operating conditions of practical PEMFCs. As shown in the j–V polarization curves (**Figure 4**a), the performances of the RCMs containing antioxidants were lower than that of pristine one. This slight performance loss originates from the degradation of proton conductivity due to the additive. The electrochemical impedance spectroscopy (EIS) data of the RCMs at 0.6 V also indicated increased ohmic resistance in the antioxidant-based RCMs compared to the pristine case (Figure S15, Supporting Information). In detail, the CNP@DSA-RCM showed the lowest performance loss among the antioxidant-based RCMs. The CNP@DSA-RCM exhibited 1.38 A cm^{-2} of current density at 0.6 V of cell voltage ($j_{0.6 V}$), which was higher than those of the Ce(III) salt (1.30 A cm^{-2}) and CNP@TTAB (0.73 A cm^{-2})-based RCM. In the mass transport region, the performance of CNP@DSA-RCM was even comparable to the pristine sample, while the RCMs based on the Ce(III) salt or CNP@TTAB showed much lower cell performance. As shown in Figure 4b, the maximum power density (p_{Max}) of the CNP@DSA-RCM (1.07 W cm^{-2}) surpassed that of the Ce(III) salt-RCM (0.89 W cm^{-2}) and CNP@TTAB-RCM (0.69 W cm^{-2}), rivaling that of the pristine sample (1.13 W cm^{-2}). The performance loss also stems from the contamination of the cathode layer in MEAs by disintegrated Ce species. We performed Tafel analyses to gain insight into the mechanism of the oxygen reduction reaction (ORR) for the cathodes of each MEA. To obtain Tafel plots, we measured j–V polarization curves by supplying H$_2$ and O$_2$. As shown in Figure S16 (Supporting Information), RCMs containing antioxidants exhibit higher values of Tafel slopes than pristine RCM, implying that introducing antioxidants alters the rate-determining steps of ORR. This alteration can emanate from the migration of Ce species in RCM toward cathode layers by electroosmotic drag. The migrated Ce species often block the catalytic surface of cathode layers and degrade the catalytic reaction. Notably, among the antioxidant-based RCMs, CNP@DSA-RCM exhibits the lowest Tafel slope. It suggests that the Ce contamination by CNP@DSA is lower than others, implying high stability of CNP@DSA induced from DSA capping. We also compared the PEMFC performance of the CNP@DSA-RCM with those of previously reported antioxidant-based MEAs (Table S2, Supporting Information). Table S2 (Supporting Information) indicates that the CNP@DSA based MEA was one of the best-performing MEAs, corroborating the excellent antioxidation efficiency of CNP@DSA. In addition, in RH 30%, CNP@DSA delivered the highest cell performance and the lowest ohmic resistance (Figure S17, Supporting Information) among the prepared RCMs. We note that the enhanced antioxidation efficiency and chemical durability of the CNPs produced by the catechol groups enabled the superior cell performance of the
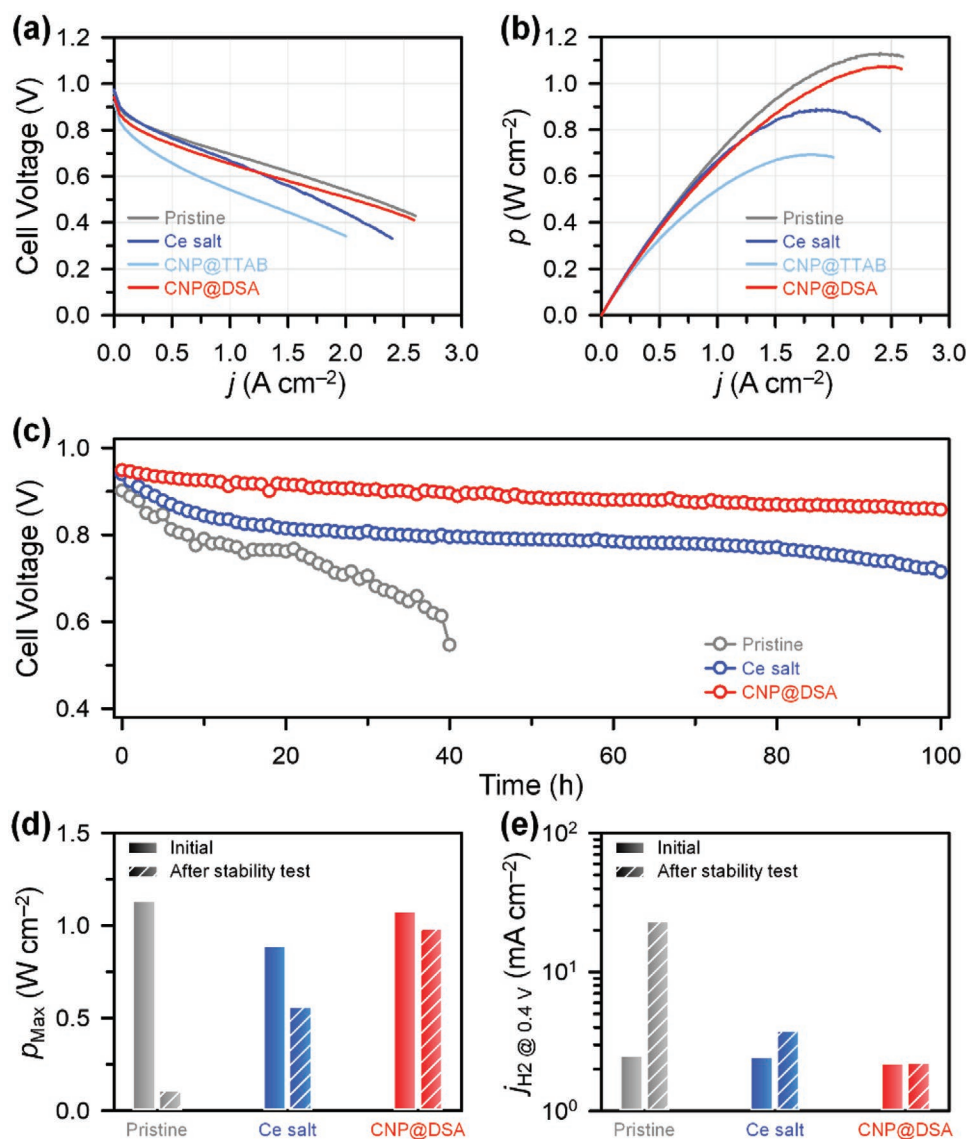
Figure 4. PEMFC performance of prepared RCM-based MEAs. a) j–V polarization curves and b) power density curves of RCM-based PEMFCs. c) OCV profile during the accelerated durability test (OCV holding for 100 h). d) Maximum power densities (p_{Max}) of RCM-based PEMFCs before and after the OCV holding stability test for 100 h. e) H_2 crossover current densities at 0.4 V (j_{H2} @ 0.4 V) of RCM-based PEMFCs before and after the OCV holding test for 100 h.

CNP@DSA-RCM. We highlight the colloidal stability of the CNPs in relation to the surface charge of the capping agents. Even though each CNP@DPL possessed similar radical scavenging activity with virtually identical FERs in the Fenton's test, they delivered dissimilar $j_{0.6\,V}$ and p_{Max} due to their different surface charges (Figure S18, Supporting Information). The trend in the ohmic resistance of the samples, as shown in the EIS data, was also in good agreement with the trend of cell performance (Figure S19, Supporting Information). These findings suggest that the high PEMFC performance of the radical scavenger-based RCM is based on the simultaneous contributions of antioxidation efficiency, chemical durability, and colloidal stability.

We further corroborated the efficient antioxidation behavior of the CNP@DSA with a PEMFC accelerated durability test (ADT).

The ADT was conducted with an open-circuit voltage (OCV) holding protocol at 90 °C with 30% RH for 100 h. Under these conditions, radical species are readily produced and promptly disintegrate the membrane backbone structure.[57,58] Figure 4c shows the gradual OCV degradation of each RCM during the ADT. The pristine RCM exhibited a drastic OCV drop from 0.940 to 0.546 V after only 40 h. The Ce(III) salt-RCM exhibited better durability than the pristine one, retaining 0.714 V of OCV after 100 h. Importantly, the CNP@DSA-RCM exhibited the lowest performance loss, maintaining 0.857 V of OCV even after 100 h. The j–V polarization curves after the ADT (Figure S20, Supporting Information) also clearly demonstrated the superior durability of the CNP@DSA-RCM over other RCMs. The preserved $j_{0.6\,V}$ of the CNP@DSA-RCM was 0.97 A cm^{-2}, which is much higher than the Ce(III) salt-RCM (0.47 A cm^{-2}).

The pristine RCM could not deliver current density after the ADT. A comparison of p_{Max} before and after the durability test (Figure 4d) also clearly confirmed that the CNP@DSA-RCM had the highest cell durability. The CNP@DSA-RCM retained 91.4% of the initial cell p_{Max}, while the Ce(III) salt-RCM (63.2%) and pristine one (9.7%) had a much lower performance. We further tested the degree of membrane disintegration with an H_2-crossover test by measuring the H_2 oxidation current density (j_{H2}) at the PEMFC cathodes. The H_2-crossover test also indicated that the CNP@DSA-RCM had the highest durability.[59,60] As indicated in Figure S21 (Supporting Information), the pristine RCM underwent a dramatic increase in j_{H2} after the ADT (40 h), while the RCMs containing antioxidants retained their initial j_{H2} even after 100 h ADT. The detailed comparison of j_{H2} at 0.4 V further revealed that the CNP@DSA-RCM had the lowest change in j_{H2}, authenticating the outstanding antioxidation efficiency of the CNP@DSA-RCM (Figure 4e).

3. Conclusion

In summary, we developed charge modulated CNPs using tailor-made charged DPLs and studied their effect on the radical scavenging process in depth. Using DLS, XPS, and PL analyses, we found that the DPLs can improve colloidal stability, chemical durability, and radical scavenging activity. They generated abundant Ce(III) active sites and prevented the loss of Ce(III)-rich surfaces against the PEMFC environment by assisting facile Ce(III) regeneration. These behaviors of the CNP@DPLs originate from the catechol ligands, which enable a synergistic radical scavenging process, high resistance in acidic and radical attacks, and enhanced water adsorption. We also determined the effect of CNP surface charge on the physicochemical properties of the RCMs and the PEMFC performance. The negatively charged CNP@DSAs exhibited the best compatibility with PEMs and the highest antioxidation efficiency in the Fenton's test. At the same time, the CNP@DSA-RCM showed excellent PEMFC performance, rivaling that of pristine RCM. The performance comparison demonstrated that the CNP@DSA-based MEA was one of the best-performing among previously reported antioxidant-based MEAs. The CNP@DSA-based PEMFC also demonstrated outstanding durability. We anticipate that our efforts to upgrade the CNP surface will provide new approaches for designing highly active and durable PEMFCs. Additionally, the surface engineering method can be extended to various other fields, including catalytic, electronic, and biological applications.

4. Experimental Section

Materials: All chemicals and solvents were of reagent quality and used without further purification. Cerium(III) nitrate hexahydrate (Ce(NO$_3$)$_3$·6H$_2$O, >99.999%), *tert*-butylamine, ((CH$_3$)$_3$CNH$_2$, >99.5%), oleic acid (OA; CH$_3$(CH$_2$)$_7$CH=CH(CH$_2$)$_7$COOH, >99%), 4,4′-azobis (4-cyanovaleric acid) (ACVA), 2-acrylamido-2-methyl-1-propanesulfonic acid (ASA), poly(ethylene glycol) methyl ether acrylate (APEG, average M_n = 480), 2-cyano-2-propyl benzodithioate (CPB), 6-carboxyl fluorescein (6-CFL, 97% HPLC grade), isopropanol, tetradecyltrimethylammonium bromide (TTAB), and 2-(2-aminoethoxy)ethanol (AEE) were purchased from Sigma Aldrich. (3-Acrylamidopropyl)trimethylammonium chloride (ATMA) solution (74%–76% in water) was purchased from TCI. Dopamine-methacrylamide (DMA) and dibenzyl trithiocarbonate (DTC) were synthesized as previously reported.[61] Azobisisobutyronitrile (AIBN) were obtained from Junsei. 2,2,2-Trifluoroethanol (TFE, >99%) was purchased from Alfa Aesar. Organic solvents were obtained from Samchun Chemicals. Porous polytetrafluoroethylene films (PTFE, Donaldson) and PFSA ionomer (E-1669D, 3M) were prepared for the reinforced composite membranes. Hydrogen peroxide (30% H$_2$O$_2$ solution, Daejung Chemicals & Metals Co.) and iron(II) sulfate heptahydrate (FeSO$_4$·7H$_2$O, >98%, Sigma-Aldrich) were used for the Fenton's reagent.

Synthesis of CNP@OA: CNP@OA were synthesized according to a previously reported method with some modification.[26] 217.6 mg of Ce(NO$_3$)$_3$·6H$_2$O was dissolved in 15 mL of distilled water (DI water) and added into a PTFE vessel for hydrothermal synthesis. An organic solution composed of 1.2 mL of oleic acid, 0.3 mL of *tert*-butylamine, and 15 mL of toluene was carefully injected into the PTFE vessel using a syringe. After the addition of the organic solution, the PTFE vessel was sealed and transferred into an autoclave reactor. Then, the autoclave was heated at 180 °C for 24 h. After heating the autoclave, the organic solution containing as-synthesized CNP@OA was collected using a pipette. Finally, the collected CNP@OA was washed with toluene using a centrifuge at 8000 rpm for 10 min several times and redispersed in 20 mL of toluene.

Synthesis of TTAB-Capped CNPs: CNP@TTAB were prepared with a simple ligand exchange method. 5 mL of oleic CNP@OA toluene dispersion was mixed with 40 mL of aqueous solution containing 1.08 g of TTAB using an ultrasonicating mixer. Then, the mixture was heated at 65 °C to evaporate the toluene. Finally, the as-prepared CNP@TTAB aqueous dispersion was washed with DI water several times and redispersed 20 mL of in DI water.

Synthesis of DTMA: DMA (0.6 mmol), ATMA (2.4 mmol), CPB (0.15 mmol), and ACVA (0.075 mmol) were mixed in a 10 mL vial and dissolved in 2 mL of TFE and methanol. The resulting mixture was transferred to an ampule. The freeze-pump-thaw procedure was repeated three times, followed by sealing with a gas torch under vacuum and reacting in an oil bath at 70 °C for 12 h. After the reaction, the crude solution was precipitated with acetone and washed three times.

Synthesis of DmP and DSA: DMA (0.6 mmol), APEG (2.4 mmol), DTC (0.15 mmol), and AIBN (0.075 mmol) were mixed in a 10 mL vial and dissolved in 2 mL of dimethylformamide (DMF). In case of preparation of DSA, ASA substituted for the APEG monomer. The resulting mixture was transferred to an ampule and the ampule was subjected to three cycles of freeze-pump-thaw, followed by sealing with a gas torch under vacuum and reacting in an oil bath at 70 °C for 12 h. After the reaction, the crude solution was precipitated with diethyl ether and washed three times.

Surface Passivation of CNPs: To fabricate CNP@DmP, a ligand exchange method was exploited. 1 mg of oleic acid capped ceria NPs dispersed in 100 µL of tetrahydrofuran (THF) was added to 10 mg of DmP and 30 mg of AEE in 300 ul of THF, and then, the mixture was stirred at 50 °C overnight. The crude solution was precipitated in diethyl ether after reaction and the resulted precipitated pellet was dispersed in distilled water. Excess polymeric ligand was removed using centrifugal filters (Millipore, M_w cutoff = 50 kDa). CNP@DTMA and CNP@DSA were prepared by a biphasic ligand exchange method with CHCl$_3$, D.W., and TFE. 1 mg of oleic acid capped CNPs dispersed in 200 µL of CHCl$_3$ was added to 10 mg of DTMA or DSA, 30 mg of AEE in 200 µL of TFE and 50 µL distilled water. Then, the mixture was stirred at 50 °C overnight. After reaction, upper layer was transferred into another vessel and precipitated with acetone. Distilled water was added to disperse the precipitate and excess ligand was removed using centrifugal filters (Millipore, M_w cutoff = 50 kDa).

Characterization Methods: TEM analyses were performed using FEI Tecnai (Thermo Fisher Scientific) at an acceleration voltage of 200 kV. The Ce contents in the catalysts were analyzed using an inductively coupled plasma optical emission spectroscopy analyzer (700-ES, Varian). The

particle size of prepared nanostructures was estimated using DLS analyses. XPS spectra were acquired using an X-ray photoelectron spectrometer (ESCALAB 250XI, Thermo Fisher Scientific) with a monochromatic Al Kα X-ray source (1486.6 eV). XPS spectra were deconvoluted using XPSPeak41 software with a mixed Gaussian (70)–Lorentzian (30) function after Shirley-type background correction. The UV–vis spectroscopy was measured under irradiation from 600 to 350 nm. The UV–vis analytes were prepared by adding the H_2O_2 solution of various concentrations (0, 0.1, 0.5, 1, 3, 30, 50, 100, 500, 1000 $\times 10^{-3}$ M) into the red-colored CNP@DSA aqueous dispersion (30×10^{-3} M) at room temperature.[49]

PL Measurement: Fenton's solution was prepared by mixing 75 mL H_2O_2 (30 wt% solution) and 18.7 mg $FeSO_4 \cdot 7H_2O$ in 250 mL distilled water. Also, a solution of fluorescent dye, 6-CFL, was prepared by dissolving 0.1 mg of the 6-CFL dye in 1 mL of isopropanol. After stirring the Fenton's reagent for 15 min, antioxidants were added to the solution of Fenton's reagent. The added amounts of CNPs for each sample were identical. Immediately after adding CNPs, 0.2 mL of the dye solution was added to 4.8 mL of the Fenton's reagent. Then, the PL spectra were measured over time (up to 200–300 min) using a fluorescence spectrometer (StellarNet) with photoexcitation at 390 nm.

Fabrication of RCMs: RCMs were fabricated by modifying the roll-to-roll process.[5] To impregnate the antioxidants in the RCM, 8.5 mL of aqueous dispersion was mixed with 10.6 mL of isopropanol, 1 mL of ethanol, and 3 g of PFSA ionomer. Typically, the amount of antioxidant was determined to adjust 0.2 mol% of $[Ce]/[SO_3^-]$. The antioxidant-PFSA mixture was stirred at room temperature for 24 h for the even dispersion. Then, the as-prepared dispersion of antioxidant–PFSA mixture was impregnated into the top and bottom sides of the porous PTFE film, using a micrometer film applicator. Then, the composite film was dried in an oven at 80 °C for about 16 h. The dried RCM was carefully separated from the glass plate. Finally, the separated RCM was heated at 150 °C for 30 min prior to use.

Physicochemical Characterization of RCMs: Cross-sectional images of samples were obtained with field-emission scanning electron microscopy (FESEM; FEI Teneo Volume Scope, Thermo-Fisher Scientific) at an activation voltage of 10 kV. All samples were coated with a Pt layer by sputter coating. Tensile strength tests were performed to confirm the mechanical properties of the RCMs. After fixing a rectangular dried RCMs (10 mm $\times$ 40 mm) in a tensile tester, the yield strength and ultimate strength were measured while applying a crosshead displacement rate of 10 mm min^{-1} at a gauge length of 20 mm at ambient conditions, including room temperature. The water uptake of RCMs was calculated by the following equation (water uptake $= m_{wet}/m - 1$), where m_{wet} is the weight of the RCM adsorbed with DI water for 24 h, and m is the weight of the dry RCM.[62] The chemical durability of the prepared composite membranes was estimated using a Fenton's test. The fresh composite membranes were dried and weighed, and then immersed into a 30 mL Fenton solution (2 wt% H_2O_2, 3 ppm Fe(II)) at 80 °C. An ion chromatography system (Orion Star A214, Thermo Scientific) was used to detect the concentration of the fluoride ions in the Fenton's solution.

Fabrication of MEAs: The membrane electrode assemblies were fabricated using the following processes with the prepared composite membranes. The active area of MEAs was controlled as 5 cm^2. Pt/C catalyst (Pt 46.5 wt%, Tanaka K. K.) and Nafion ionomer solution were added to isopropanol and catalyst solutions and were ultrasonicated for 30 min. The MEA was assembled into fuel cell stack model for testing. Catalyst loading was 0.2 mg$_{Pt}$ cm^{-2} for the anode and 0.4 mg$_{Pt}$ cm^{-2} for the cathode. Finally, the MEAs were sandwiched between two gas diffusion layers (GDL, 39BC, Sigracet SGL Carbon Inc.) and gaskets (Teflon).

Electrochemical Measurement: For electrochemical analyses, the single cell was installed in a fuel cell test station (CNL). The j–V polarization curves were measured repetitively from OCV to 0.4V in potentiodynamic mode, at a scan rate of 20 mV s^{-1}. Before measuring the performance, the single cell was activated under a constant voltage operation of 0.4 V. The typical cell operating temperature and RH was 80 °C and 50%, respectively. The supply of hydrogen and air to the anode and cathode is at 0.2 and 0.6 L min^{-1}, respectively, with 0.8 bar of backpressure. Electrochemical properties were examined using a potentiostat

(Solartron Analytical). For better understanding of ionic resistance, EIS was performed (IM6, Zahner Elektrik GmbH) at 0.6 V with an amplitude of 10 mV.[63–66] The measurement was conducted over the frequency range of 70 kHz to 0.1 Hz, after purging with H_2 anode gas and N_2 cathode gas. For the Tafel analysis, the cell performance was tested by supplying hydrogen and oxygen gases, with 0.8 bar of backpressure. After obtaining j–V polarization curves, high-frequency resistance (HFR) was measured with EIS at the frequency range of 1 MHz to 0.5 Hz according to current density. Linear sweep voltammetry was carried out between 0.05 and 0.6 V at 2 mV s^{-1}, with H_2 as the anode gas and N_2 as the cathode gas. H_2-crossover was determined at a current density at 0.4 V.

Supporting Information

Supporting Information is available from the Wiley Online Library or from the author.

Conflict of Interest

The authors declare no conflict of interest.

Data Availability Statement

The data that support the findings of this study are available from the corresponding author upon reasonable request.

[1] M. S. Whittingham, R. F. Savinell, T. Zawodzinski, *Chem. Rev.* **2004**, *104*, 4243.

[2] A. Kusoglu, A. Z. Weber, *Chem. Rev.* **2017**, *117*, 987.

[3] L. Gubler, W. H. Koppenol, *J. Electrochem. Soc.* **2011**, *159*, B211.

[4] M. Breitwieser, C. Klose, A. Hartmann, A. Büchler, M. Klingele, S. Vierrath, R. Zengerle, S. Thiele, *Adv. Energy Mater.* **2017**, *7*, 1602100.

[5] K. R. Yoon, K. A. Lee, S. Jo, S. H. Yook, K. Y. Lee, I.-D. Kim, J. Y. Kim, *Adv. Funct. Mater.* **2019**, *29*, 1806929.

[6] A. M. Baker, A. R. Crothers, K. Chintam, X. Luo, A. Z. Weber, R. L. Borup, A. Kusoglu, *ACS Appl. Polym. Mater.* **2020**, *2*, 3642.

[7] A. M. Baker, R. Mukundan, D. Spernjak, E. J. Judge, S. G. Advani, A. K. Prasad, R. L. Borup, *J. Electrochem. Soc.* **2016**, *163*, F1023.

[8] A. M. Baker, S. T. D. Williams, R. Mukundan, D. Spernjak, S. G. Advani, A. K. Prasad, R. L. Borup, *J. Mater. Chem. A* **2017**, *5*, 15073.

[9] R. Singh, P. C. Sui, K. H. Wong, E. Kjeang, S. Knights, N. Djilali, *J. Electrochem. Soc.* **2018**, *165*, F3328.

[10] T. Weissbach, T. J. Peckham, S. Holdcroft, *J. Membr. Sci.* **2016**, *498*, 94.

[11] S. Yuk, D. W. Lee, K.-Y. Song, S. Choi, D.-H. Lee, G. Doo, J. Hyun, J. Kwen, J. Y. Kim, H.-T. Kim, *J. Power Sources* **2020**, *448*, 227447.

[12] J. Kim, K. Chung, H. Lee, B. Bae, E.-B. Cho, *Microporous Mesoporous Mater.* **2016**, *236*, 292.

[13] S. S. Lee, W. Song, M. Cho, H. L. Puppala, P. Nguyen, H. Zhu, L. Segatori, V. L. Colvin, *ACS Nano* **2013**, *7*, 9693.

[14] B. P. Pearman, N. Mohajeri, D. K. Slattery, M. D. Hampton, S. Seal, D. A. Cullen, *Polym. Degrad. Stab.* **2013**, *98*, 1766.

[15] K. Ketpang, K. Oh, S.-C. Lim, S. Shanmugam, *J. Power Sources* **2016**, *329*, 441.

[16] N. N. Krishnan, D. Henkensmeier, J. H. Jang, H.-J. Kim, *Macromol. Mater. Eng.* **2014**, *299*, 1031.

[17] M. A. Boles, D. Ling, T. Hyeon, D. V. Talapin, *Nat. Mater.* **2016**, *15*, 141.

[18] C. D'Urso, C. Oldani, V. Baglio, L. Merlo, A. S. Aricò, *J. Power Sources* **2016**, *301*, 317.

[19] Y. Xue, Q. Luan, D. Yang, X. Yao, K. Zhou, *J. Phys. Chem. C* **2011**, *115*, 4433.

[20] A. Donnadio, R. D'Amato, F. Marmottini, G. Panzetta, M. Pica, C. Battocchio, D. Capitani, F. Ziarelli, M. Casciola, *J. Membr. Sci.* **2019**, *574*, 17.

[21] H. B. Na, G. Palui, J. T. Rosenberg, X. Ji, S. C. Grant, H. Mattoussi, *ACS Nano* **2011**, *6*, 389.

[22] E. Amstad, M. Textor, E. Reimhult, *Nanoscale* **2011**, *3*, 2819.

[23] C. Cao, E. Kim, Y. Liu, M. Kang, J. Li, J.-J. Yin, H. Liu, X. Qu, C. Liu, W. E. Bentley, G. F. Payne, *Biomacromolecules* **2018**, *19*, 3502.

[24] G. B. Bubols, D. da Rocha Vianna, A. Medina-Remon, G. von Poser, R. M. Lamuela-Raventos, V. L. Eifler-Lima, S. C. Garcia, *Mini-Rev. Med. Chem.* **2013**, *13*, 318.

[25] S. Manchineella, C. Voshavar, T. Govindaraju, *Eur. J. Org. Chem.* **2017**, *2017*, 4363.

[26] F. Dang, K. Kato, H. Imai, S. Wada, H. Haneda, M. Kuwabara, *Cryst. Growth Des.* **2010**, *10*, 4537.

[27] A. Krishnan, T. S. Sreeremya, A. P. Mohamed, U. S. Hareesh, S. Ghosh, *RSC Adv.* **2015**, *5*, 23965.

[28] M. A. M. Khan, W. Khan, M. Ahamed, A. N. Alhazaa, *Sci. Rep.* **2017**, *7*, 12560.

[29] H. Kim, H. Kim, S. H. Kim, J. M. Park, Y. J. Jung, S. K. Kwak, J. Park, *Chem. Mater.* **2021**, *33*, 952.

[30] D. Ling, W. Park, Y. I. Park, N. Lee, F. Li, C. Song, S.-G. Yang, S. H. Choi, K. Na, T. Hyeon, *Angew. Chem., Int. Ed.* **2011**, *50*, 11360.

[31] J. Zeng, L. Jing, Y. Hou, M. Jiao, R. Qiao, Q. Jia, C. Liu, F. Fang, H. Lei, M. Gao, *Adv. Mater.* **2014**, *26*, 2694.

[32] J. Yu, W. Wei, M. S. Menyo, A. Masic, J. H. Waite, J. N. Israelachvili, *Biomacromolecules* **2013**, *14*, 1072.

[33] W. Lin, J. Walter, A. Burger, H. Maid, A. Hirsch, W. Peukert, D. A. Segets, *Chem. Mater.* **2015**, *27*, 358.

[34] A. K. L. Yuen, G. A. Hutton, A. F. Masters, T. Maschmeyer, *Dalton Trans.* **2012**, *41*, 2545.

[35] M. D. Shultz, J. U. Reveles, S. N. Khanna, E. E. Carpenter, *J. Am. Chem. Soc.* **2007**, *129*, 2482.

[36] E. Amstad, T. Gillich, I. Bilecka, M. Textor, E. Reimhult, *Nano Lett.* **2009**, *9*, 4042.

[37] C. Liu, P. M. Huang, *Org. Geochem.* **2002**, *33*, 295.

[38] A. Hayat, D. Andreescu, G. Bulbul, S. Andreescu, *J. Colloid Interface Sci.* **2014**, *418*, 240.

[39] M. Jabbari, F. Gharib, *Monatsh. Chem.* **2012**, *143*, 997.

[40] D. Banham, S. Ye, T. Cheng, S. Knights, S. M. Stewart, M. Wilson, F. Garzon, *J. Electrochem. Soc.* **2014**, *161*, F1075.

[41] D. Channei, S. Phanichphant, A. Nakaruk, S. S. Mofarah, P. Koshy, C. C. Sorrell, *Catalysts* **2017**, *7*, 45.

[42] S. H. Yook, H. Y. Kim, S. J. Kim, S. Choi, T. Kwon, H. Cho, J. M. Kim, K. R. Yoon, S. Jo, S. Y. Lee, H.-J. Kim, H. J. Son, K. H. Chae, J. Kim, K. Y. Lee, J. Y. Kim, *Chem. Eng. J.* **2022**, *432*, 134419.

[43] M. S. Menyo, C. J. Hawker, J. H. Waite, *Soft Matter* **2013**, *9*, 10314.

[44] V. Baldim, F. Bedioui, N. Mignet, I. Margaill, J. F. Berret, *Nanoscale* **2018**, *10*, 6971.

[45] J. Kim, J. E. Lee, J. Lee, J. H. Yu, B. C. Kim, K. An, Y. Hwang, C.-H. Shin, J.-G. Park, J. Kim, T. Hyeon, *J. Am. Chem. Soc.* **2006**, *128*, 688.

[46] N. Zhu, H. Ji, P. Yu, J. Niu, M. U. Farooq, M. W. Akram, I. O. Udego, H. Li, X. Niu, *Nanomaterials* **2018**, *8*, 810.

[47] M. Asgari, M. Soleymani, T. Miri, A. Barati, *J. Mol. Liq.* **2019**, *292*, 111367.

[48] S. M. Louie, R. D. Tilton, G. V. Lowry, *Environ. Sci. Nano* **2016**, *3*, 283.

[49] C. K. Kim, T. Kim, I.-Y. Choi, M. Soh, D. Kim, Y.-J. Kim, H. Jang, H.-S. Yang, J. Y. Kim, H.-K. Park, S. P. Park, S. Park, T. Yu, B.-W. Yoon, S.-H. Lee, T. Hyeon, *Angew. Chem., Int. Ed.* **2012**, *51*, 11039.

[50] T.-C. Jao, G.-B. Jung, S.-C. Kuo, W.-J. Tzeng, A. Su, *Int. J. Hydrogen Energy* **2012**, *37*, 13623.

[51] S. Rose, A. Prevoteau, P. Elziere, D. Hourdet, A. Marcellan, L. Leibler, *Nature* **2014**, *505*, 382.

[52] S. Xiao, H. Zhang, C. Bi, Y. Zhang, Y. Ma, X. Li, H. Zhong, Y. Zhang, *J. Power Sources* **2010**, *195*, 8000.

[53] S. Hong, J. S. Lee, J. Ryu, S. H. Lee, D. Y. Lee, D.-P. Kim, C. B. Park, H. Lee, *Nanotechnology* **2011**, *22*, 494020.

[54] J. Ryu, S. H. Ku, H. Lee, C. B. Park, *Adv. Funct. Mater.* **2010**, *20*, 2132.

[55] J. Hou, J. Li, D. Mountz, M. Hull, L. A. Madsen, *J. Membr. Sci.* **2013**, *448*, 292.

[56] X.-Y. Zheng, K. Zhao, J. Tang, X.-Y. Wang, L.-D. Li, N.-X. Chen, Y.-J. Wang, S. Shi, X. Zhang, S. Malaisamy, L.-D. Sun, X. Wang, C. Chen, C.-H. Yan, *ACS Nano* **2017**, *11*, 3642.

[57] E. Endoh, S. Terazono, H. Widjaja, Y. Takimoto, *Electrochem. Solid-State Lett.* **2004**, *7*, A209.

[58] E. Endoh, *ECS Trans.* **2008**, *16*, 1229.

[59] L. Carrette, K. A. Friedrich, U. Stimming, *Fuel Cells* **2001**, *1*, 5.

[60] M. Schoemaker, U. Misz, P. Beckhaus, A. Heinzel, *Fuel Cells* **2014**, *14*, 412.

[61] N. Aoyagi, T. Endo, *J. Polym. Sci., Part A: Polym. Chem.* **2009**, *47*, 3702.

[62] J. Peron, A. Mani, X. Zhao, D. Edwards, M. Adachi, T. Soboleva, Z. Shi, Z. Xie, T. Navessin, S. Holdcroft, *J. Membr. Sci.* **2010**, *356*, 44.

[63] T. Gaumont, G. Maranzana, O. Lottin, J. Dillet, S. Didierjean, J. Pauchet, L. Guétaz, *Int. J. Hydrogen Energy* **2017**, *42*, 1800.

[64] G. Li, P. G. Pickup, *J. Electrochem. Soc.* **2003**, *150*, C745.

[65] D. Malevich, B. R. Jayasankar, E. Halliop, J. G. Pharoah, B. A. Peppley, K. Karan, *J. Electrochem. Soc.* **2012**, *159*, F888.

[66] J. W. Lim, Y.-H. Cho, M. Ahn, D. Y. Chung, Y.-H. Cho, N. Jung, Y. S. Kang, O.-H. Kim, M. J. Lee, M. Kim, *J. Electrochem. Soc.* **2012**, *159*, B378.